A Technique to Evaluate MRI-Induced Electric Fields at the Ends of Practical Implanted Lead

Shi Feng, *Member, IEEE*, Rui Qiang, *Member, IEEE*, Wolfgang Kainz, *Member, IEEE*, and Ji Chen, *Member, IEEE*

***Abstract*—This paper presents a novel technique for efficient evaluation of magnetic resonance imaging (MRI)-induced electric fields or induced voltages in the vicinity of implanted metallic leads. The technique is based on the reciprocity theorem in conjunction with the Huygens Principle. This approach allows one to decouple the micro-scale metallic lead simulation/measurement from the macro-level phantom human simulations within the MRI scanners. Consequently, the estimation of MRI-induced heating on an implanted lead, and the induced voltage on the pacemaker device can be greatly simplified. In addition, this method clearly explains the induced lead heating mechanism during MRI procedures. Several numerical examples, as well as measurement results are given to demonstrate the efficiency and accuracy of this method.**

***Index Terms*—Magnetic resonance imaging (MRI), pacemaker, reciprocity, transfer functions.**

I. Introduction

IT IS estimated that on average 100% of the U.S. population will receive one magnetic resonance imaging (MRI) exam in their lifetime. Cardiologists and radiologists have anticipated that three out of four patients with a pacemaker or defibrillator will need an MRI scan during the lifetime of their devices. However, patients currently with implanted medical devices, such as pacemakers and defibrillators, are restricted from undergoing an MRI because of serious concerns for tissue damage due to the lead tip heating, induced arrhythmias, and electromagnetic compatibility (EMC) issues [1].

The concern for tissue damage comes from local tissue temperature increase in the vicinity of the implanted lead tip. During MRI procedures, the electromagnetic fields emitted by an RF coil penetrate into patients and interact with human tissues. If a metallic lead is present within the tissue, the induced RF signals propagate along the leads and deposit the induced energy at the lead tip electrode area, causing significant local temperature rise. Such a large local temperature increase could exceed the safety limits for surrounding tissues [2]. In some cases, the local temperature rise can exceed 30 °C, which can cause instant tissue damage [3].

To understand MRI-induced heating on the implanted metallic lead, both carefully designed experiments and advanced electromagnetic simulations were performed by various groups [4]–[23]. Experiments were mostly performed on phantoms, such as the ASTM phantom [9]–[12] and then validated using actual human or animal studies. The electromagnetic simulations were also carried out on detailed anatomical human models [9]–[16]. In particular, the transfer function concept was proposed based on the transmission line approach; however, the theoretical framework has yet to be established [13]. With recent advances in human model development, we are now able to obtain electromagnetic field distributions at millimeter resolution [24]. This provides the potential of human bodies using electromagnetic modeling to understand the *in-vivo* MRI-induced heating on the implanted medical devices. In [17], simplified deep brain stimulation leads were modeled using thin wire models. However, such study is only limited to 1-mm resolution on a head model only, and it required simulations over two days. For other leads with sub-millimeter features, such direct modeling can be extremely challenging.

Therefore, even with current state-of-the-art electromagnetic modeling algorithms such as the finite-difference time-domain (FDTD) method, it is still computationally prohibitive to model the entire MRI RF body coil, the human anatomical model, and implanted metallic leads in sufficient resolution simultaneously. This is due to the dimension differences between the metallic lead, the MRI RF coil, and the human body. The dimensions of a typical MRI RF body coil are on the order of meters, while the size of the implanted lead is on the order of sub-millimeters. Therefore, to model the MRI coil, the anatomical human model and metallic lead with sub-millimeter features, significant computational resources, such as computer memory, are required, even when nonuniform meshes are applied. In addition, even if there is sufficient computer memory to accommodate the entire computational domain, the tiny mesh size used for the lead modeling limits the time-step size in FDTD simulations. For example, if one uses 0.1-mm resolution grid size to model the implanted lead, the maximum time step one can use is on the order of one-tenth of a picosecond. For MRI scanners operating at either 64 MHz (1.5T) or 128 MHz (3T), over millions of time steps are required to reach steady state. Therefore, it is very difficult to model implanted leads together with a realistic RF coil and anatomical human models practically. Consequently, only a simplified pacemaker and leads were modeled in the previous study [4].

Manuscript received April 02, 2014; revised July 11, 2014 and October 03, 2014; accepted November 20, 2014. Date of publication December 05, 2014; date of current version December 31, 2014.

S. Feng and J. Chen are with the Department of Electrical and Computer Engineering, University of Houston, Houston, TX 77204 USA (e-mail: sfeng5@uh.edu; jchen18@uh.edu).

R. Qiang is with Micro Systems Engineering Inc., Lake Oswego, OR 97035 USA.

W. Kainz is with the Food and Drug Administration (FDA), Center for Devices and Radiological Health, Silver Spring, MD 20993 USA.

Color versions of one or more of the figures in this paper are available online at http://ieeexplore.ieee.org.

Digital Object Identifier 10.1109/TMTT.2014.2376523

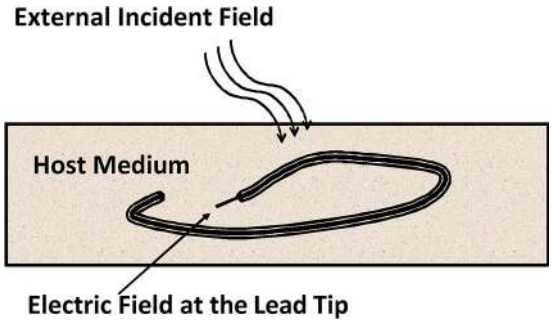

Fig. 1. Diagram representing the general implanted metallic leads exposed to an arbitrary RF source.

In this paper, we propose a novel technique to efficiently evaluate implanted lead heating inside the human body when exposed in the MRI environment. Rather than performing one comprehensive electromagnetic simulation that includes the RF coil, the anatomical human body model, and the metallic lead all together, this approach performs two independent and much simplified studies. In the first step, the lead implanted inside the anatomical human model is excluded from the simulation and the incident electric field along the lead trajectories are computed. In the second step, only the implanted lead within the small volume of surrounding tissues will be modeled/measured. The electric current distribution along the lead wire is obtained by using a reciprocity approach either through modeling or measurement. As we can see in the following sections, by appropriately integrating the incident electric field and current distribution along the lead wire, we are able to accurately evaluate the induced electric field at the lead tip electrode or the induced voltage between different conductors in a much simpler way.

This paper is organized as follows. In Section II, we will review the methodology associated with the proposed method. Detailed numerical and experimental examples are shown in Section III. Finally, conclusions are discussed in Section IV.

II. Methodology

A diagram representing the general induced electric field or induced voltage problem due to the arbitrary incident electromagnetic field is shown in Fig. 1. The metallic lead is embedded in a medium that may consist of homogeneous or inhomogeneous materials/tissues. The temperature rise at the lead tip electrode depends on the electric field near the tip, e.g., $\mathbf{E}$. Hence, obtaining $\mathbf{E}$ will provide sufficient information to evaluate the tip heating.

A. Applying Huygen's Principle

As stated in Section I, direct numerical modeling of the original problem in Fig. 1 is quite difficult due to the large size of the simulation domain and the tiny structure of the leads. To solve the problem, we need to separate the study into two parts. An artificial surface $\mathbf{S}$, which only encloses the entire lead, is chosen as shown in Fig. 2(a). According to the Huygens principle [25], the external incident source can be replaced by the equivalent surface current densities $\mathbf{J}_{s,\mathrm{inc}}$ and $\mathbf{M}_{s,\mathrm{inc}}$ defined as

$$\mathbf{J_{s,inc}} = \hat{\mathbf{n}} \times \mathbf{H}_{\mathrm{inc}} \tag{1}$$

$$\mathbf{M_{s,inc}} = -\hat{\mathbf{n}} \times \mathbf{E}_{\mathrm{inc}}. \tag{2}$$

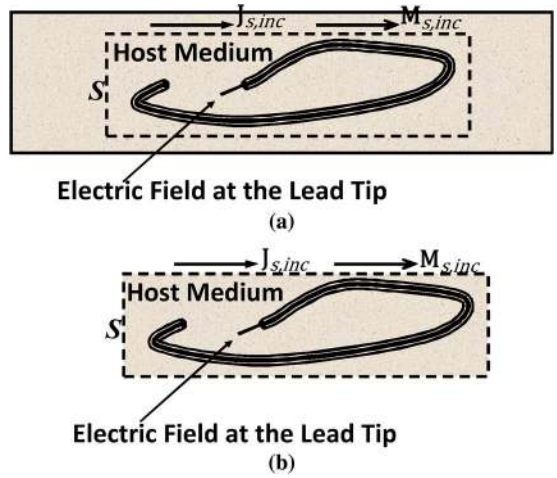

Fig. 2. Equivalent problems after applying Huygens equivalent principle. (a) External incident field is replaced by the equivalent surface current $\mathbf{J}_{s,\mathrm{inc}}$ and $\mathbf{M}_{s,\mathrm{inc}}$ on an imaginary closed surface. (b) According to equivalent principle, the medium outside the imaginary surface $\mathbf{S}$ can be considered as free space or any type of medium.

where $\mathbf{E}_{\mathrm{inc}}$ and $\mathbf{H}_{\mathrm{inc}}$ are the incident fields on the artificial surface $\mathbf{S}$. The original problem can be further reduced to Fig. 2(b) by considering the outside material to be air or free space. This indicates that we can obtain $\mathbf{E}_{\mathrm{tip}}$ using two consecutive steps, which are as follows. 1) By excluding the lead, which allows the use of a coarse mesh. The initial $\mathbf{E}_{\mathrm{tan,inc}}$ and $\mathbf{H}_{\mathrm{tan,inc}}$ on the surface $\mathbf{S}$ can then be obtained and transformed to the incident current sources in (1) and (2) for the problem in Fig. 2(b). 2) By applying the calculated equivalent sources $\mathbf{J}_{s,\mathrm{inc}}$ and $\mathbf{M}_{s,\mathrm{inc}}$, and a fine mesh inside the enclosed surface $\mathbf{S}$, which allows the detailed modeling of the lead and the lead tip, we are able to calculate $\mathbf{E}_{\mathrm{tip}}$ in a much smaller simulation domain than the original problem in Fig. 1. This approach is particularly referred to as Huygens sub-gridding for the FDTD method [26] and it may work very well with the straight lead. However, a lead usually has complex tiny structures such as a helix so that the efficiency of this method decreases dramatically. Furthermore, to obtain $\mathbf{E}_{\mathrm{tip}}$, when the lead is placed at arbitrary location, we need to calculate the incident fields for each box at different locations.

B. Applying Reciprocity Theorem

To efficiently evaluate $\mathbf{E}_{\mathrm{tip}}$, the reciprocity theorem is applied here. Two sets of sources $\mathbf{J}_1$, $\mathbf{M}_1$ and $\mathbf{J}_2$, $\mathbf{M}_2$ excited individually, which produce fields $\mathbf{E}_1$, $\mathbf{H}_1$ and $\mathbf{E}_2$, $\mathbf{H}_2$, are used. As shown in Fig. 3, the equivalent surface currents $\mathbf{J}_{s,\mathrm{inc}}$ and $\mathbf{M}_{s,\mathrm{inc}}$ are considered as the source of the first scenario of $\mathbf{J}_1$ and $\mathbf{M}_1$, and the small current source $\mathbf{J}_{\mathrm{tip}}$ placed at the lead's tip is considered as the source for the second scenario as $\mathbf{J}_2$. Since no magnetic current source is applied at the lead's tip, $\mathbf{M}_2$ is zero. The relationship between the sources and generated fields can be expressed as

$$\iiint_v \mathbf{E}_1 \cdot \mathbf{J}_2 dv = \iiint_v (\mathbf{E}_2 \cdot \mathbf{J}_1 - \mathbf{H}_2 \cdot \mathbf{M_1}) \mathbf{dv} \tag{3}$$

where the external incident field is represented by the equivalent surface currents $\mathbf{J}_1$, $\mathbf{M}_1$ and a current source $\mathbf{J}_2$ $(\mathbf{J}_{\mathrm{tip}})$ is impressed at the lead tip electrode. The tangential fields $\mathbf{E}_2$

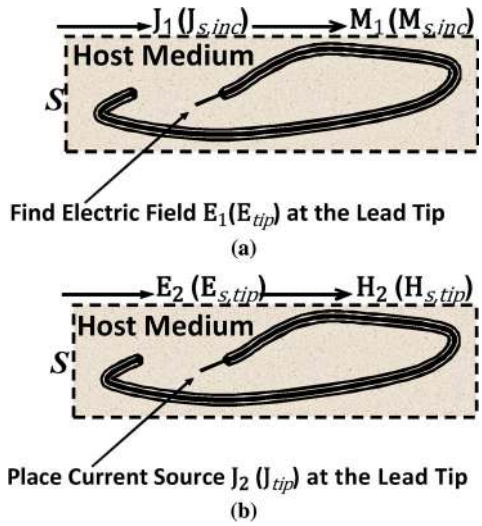

Fig. 3. Equivalent problems after applying reciprocity theorem. (a) Objective: find the electric field $\mathbf{E}_{\rm tip}$ due to equivalent surface currents $\mathbf{J}_{s,\rm inc}$ and $\mathbf{M}_{s,\rm inc}$ on the surface $\mathbf{S}$. (b) Auxiliary problem: find tangential fields $\mathbf{E}_{s,\rm tip}$ and $\mathbf{H}_{s,\rm tip}$ on the surface $\mathbf{S}$ due to current source $\mathbf{J}_{\rm tip}$ excited at the lead tip electrode.

($\mathbf{E}_{s,\rm tip}$) and $\mathbf{H}_2$ ($\mathbf{H}_{s,\rm tip}$), due to the impressed source $\mathbf{J}_{\rm tip}$, on the same artificial surface $\mathbf{S}$ are then calculated. Once $\mathbf{J}_{s,\rm inc}$, $\mathbf{M}_{s,\rm inc}$, $\mathbf{E}_{s,\rm tip}$, and $\mathbf{H}_{s,\rm tip}$ are known, we are able to calculate $\mathbf{E}_{\rm tip}$ by rewriting (3) to

$$\iiint_v \mathbf{E}_{\rm tip}\cdot\mathbf{J}_{\rm tip}dv = \oiint_s (\mathbf{E}_{s,\rm tip}\cdot\mathbf{J}_{s,\rm inc} - \mathbf{H}_{s,\rm tip}\cdot\mathbf{M}_{s,\rm inc})ds \tag{4}$$

where the right-hand side is reduced to the surface integral due to the fact that $\mathbf{J}_1$ ($\mathbf{J}_{s,\rm inc}$) and $\mathbf{M}_1$ ($\mathbf{M}_{s,\rm inc}$) are surface currents on $\mathbf{S}$. Furthermore, the current source $\mathbf{J}_{\rm tip}$ is represented as a small dipole edge source at the tip electrode, and (4) can then be reduced to

$$\mathbf{E}_{\rm tip}\cdot\mathbf{I}_{\rm tip}\Delta l_I = \oiint_s (\mathbf{E}_{s,\rm tip}\cdot\mathbf{J}_{s,\rm inc} - \mathbf{H}_{s,\rm tip}\cdot\mathbf{M}_{s,\rm inc})ds \tag{5}$$

where Δl_I is the length of the current dipole source $\mathbf{I}_{\rm tip}$. Finally, $\mathbf{E}_{\rm tip}$ can be calculated by

$$|\mathbf{E}_{\rm tip}| = \oiint_s (\mathbf{E}_{s,\rm tip}\cdot\mathbf{J}_{s,\rm inc} - \mathbf{H}_{s,\rm tip}\cdot\mathbf{M}_{s,\rm inc})\frac{ds}{|\mathbf{I}_{\rm tip}|\Delta l_I} \tag{6}$$

Solving $\mathbf{E}_{\rm tip}$ in Fig. 3(b) directly using (5) seems as difficult as solving $\mathbf{E}_{\rm tip}$ in Fig. 2(b). However, if we choose the artificial surface $\mathbf{S}$ to be the lead itself, as in Fig. 4, the integration of $\mathbf{E}_{s,\rm tip}\cdot\mathbf{J}_{s,\rm inc}$ will approach to zero as long as the lead is made of high conductivity material. For the second term, by applying Amperes Law of $\oint \mathbf{H}\cdot d\mathbf{l} = \mathbf{I}_L$ and $\mathbf{M}_s = -\hat{\mathbf{n}}\times\mathbf{E}_{\rm tan}$, the right side of (6) reduces to a line integral along the lead trajectory. Finally, the calculation of $\mathbf{E}_{\rm tip}$ in Fig. 4 can be written as a function of a line integral of the incident field $\mathbf{E}_{L,\rm inc}$ and an induced current $\mathbf{I}_L$ over the lead trajectory L

$$|\mathbf{E}_{\rm tip}| = -\oiint_s \mathbf{H}_{s,\rm tip}\cdot\mathbf{M}_{s,\rm inc}\frac{ds}{|\mathbf{I}_{\rm tip}|\Delta l_I}$$

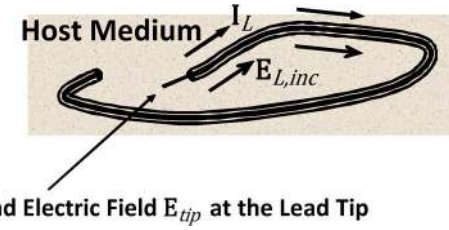

Fig. 4. Final equivalent problem after applying both reciprocity and equivalent theorems.

$$= -\int_L \frac{\mathbf{I}_L(l')\cdot\mathbf{E}_{L,\rm inc}(l')dl'}{|\mathbf{I}_{\rm tip}|\Delta l_I} \tag{7}$$

where $\mathbf{E}_{L,\rm inc}$ can be found from a simulation without the tiny leads and $\mathbf{I}_L$ is calculated or measured after impressing a small dipole source $\mathbf{I}_{\rm tip}\Delta l_I$ at the lead tip electrode, as shown in Fig. 4. As we can see in this new two-step approach, the external source influence has been successfully decoupled from the characteristics of the lead that is represented by the term $\mathbf{I}_L$. This decoupling procedure can be regarded as the first advantage of this method. By further inspection of (7), we find it quite similar as the integration formula proposed in [13], which is known as the transfer function method. However, there are actually three major differences between these two methods. 1) The integration formulas are derived from different physical interpretations. The transfer function method is based on the transmission line assumption while the method proposed here uses basic physical laws. As a result, the transfer function $\mathbf{S}_1(l')$ in the line integral formula is replaced by the term $\mathbf{I}_L(l')$ here. 2) Different excitation methods are used to find $\mathbf{S}_1(l')$ and $\mathbf{I}_L(l')$. The transfer function method requires to apply a discrete local element source at discrete positions on the lead trajectory for multiple times while this method only needs to apply a finite dipole source at the tip electrode. 3) In the transfer function method, the scattering field is finally calculated while in this method, the total field is computed.

The pacemaker leads characteristic extraction is decoupled from the actual human/phantom simulations by (7). From this derivation, the estimation of the induced electric field on the leads are divided into two steps, which are: 1) the characterization of the lead and 2) the calculation of the incident fields along different possible lead pathways inside the phantom/human models without the actual leads. Once these two steps are finished, the induced electric field from the leads along different lead pathways can be immediately evaluated using (7). For example, if one needs to evaluate the induced electric fields for a pacemaker lead along N different pathways, this approach only requires one lead characterization to obtain the $\mathbf{I}_L(l')$ and one phantom/human body simulations (to determine the electric fields along N different pathways). The induced electric fields can be evaluated immediately along all N pathways. However, if the conventional approach is used, then N electromagnetic simulations shall be performed in order to capture the induced electric fields along these pathways.

III. Numerical Examples and Experimental Validations

To validate our proposed approach, both numerical modeling and experimental measurements are used. In both approaches,

the transfer function should be obtained first through either simulation or measurement. The incident fields along different lead paths are then obtained through simulations. The transfer functions are integrated with the incident field following (7) to obtain the induced electric field. It should be pointed out that typical pacemaker leads have a very complex structure and it is not possible to obtain their transfer functions via simulations. Therefore, in the numerical modeling validation, only simple straight wires are used to demonstrate the effectiveness of our approach.

A. Numerical Validation

In numerical validation, *in-vitro* testing examples are developed and the two-step simulation discussed above is to be performed. First, we use a numerical approach to obtain the transfer function of simple wires by calculating the current distribution $\mathbf{I}_L(l')$ along the lead path. A small electric dipole source is placed at the lead tip as the excitation. Due to the conductivity loss of gel, the electric field decays very rapidly away from the metallic lead. This implies it is actually not necessary to include the MRI RF coil and the full ASTM phantom in this step. In our study, the simulation domain is reduced to a rectangular solid containing the same saline material with a size of only 18 cm $\times$ 18 cm $\times$ 90 cm. The perfectly matched layer (PML) boundary conditions are applied on its six sidewalls to truncate the FDTD simulation domain. Four different lead lengths are evaluated: L1 $=$ 43.5 cm, L2 $=$ 28.5 cm, L3 $=$ 13.5 cm, and L4 $=$ 58.5 cm, respectively. The metallic leads are modeled using the thin wire models. With this significant reduction of domain size, the minimal mesh grid size used can be much smaller than that in the second simulation, which makes it possible to model the complex lead details. This is the second advantage of our method. In the simulations, the saline has an electrical conductivity of 0.448 S/m and a relative permittivity of 80 at 64 MHz (1.5T). In all simulations, nonuniform meshes were used. In the vicinity of the wires, the mesh size is on the order of millimeters. The mesh size increases for the regions that are away from the wire. The maximum mesh size is limited within 5 mm.

In all simulations, the current distribution $\mathbf{I}_L(l')$ is calculated using $\oint \mathbf{H} \cdot d\mathbf{l} = I$ on an arbitrary closed loop around the lead cross section. With the knowledge and assumptions discussed above, the simulated magnitudes and phases of $\mathbf{I}_L(l')$ induced on these four different leads are plotted in Fig. 5. To simplify the simulations, we choose $\mathbf{I}_{\text{tip}}$ to be 1A.

Once the transfer functions are obtained, the incident fields along different pacemaker lead paths shall be evaluated. Here, a low-pass birdcage coil shown in Fig. 6 was first built as an MRI RF transmitting coil. The birdcage RF coil consists of 16 rungs, and each rung has a length of 65 cm. The diameter of the end rings is 63 cm. The coil is surrounded by a metallic shield with a diameter of 75 cm and a height of 128 cm. A phantom model described in ASTM F2182-11a [28] is then put inside this coil. The dimensions of the ASTM phantom are shown in Fig. 6. In all simulations, the quadrature excitation mode was used to excite the coil with the excitation location at the center of the rung. The input power of from the coil is normalized to

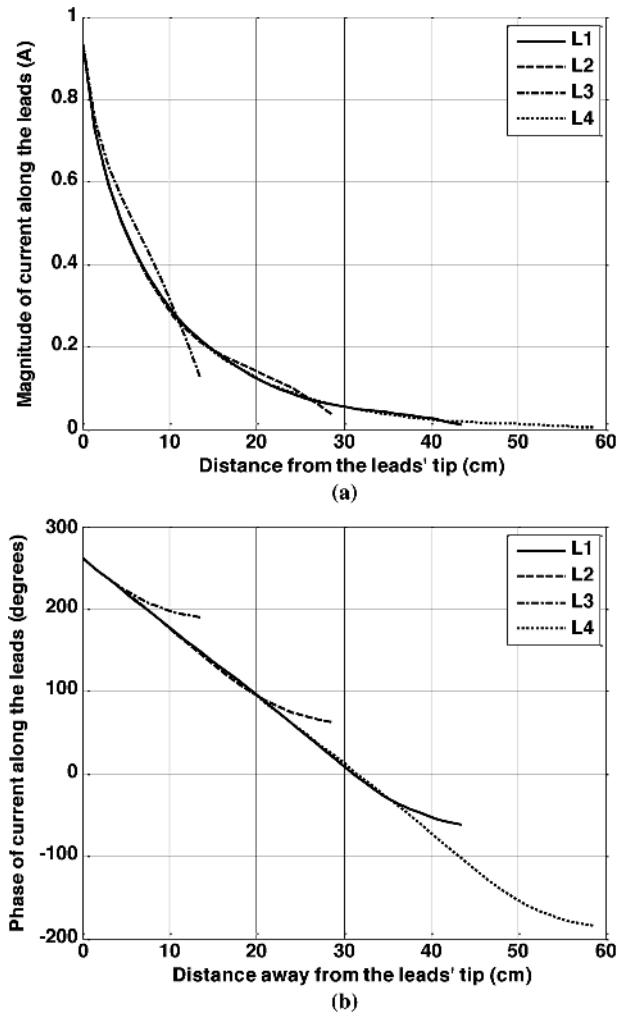

Fig. 5. (a) Magnitude and (b) unwrapped phase of the simulated induced $\mathbf{I}_L(l')$ on the straight leads for four different lengths.

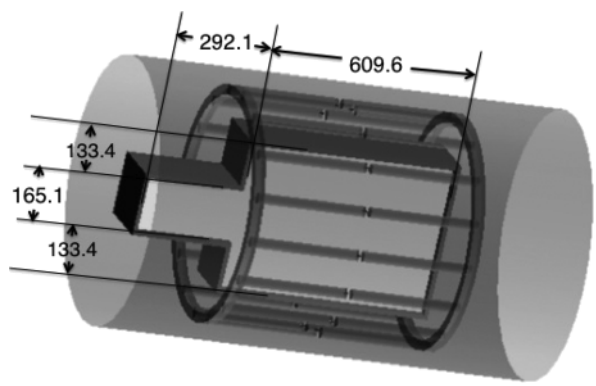

Fig. 6. ASTM phantom is loaded into a low-pass MRI RF coil. The dimensions of the phantom are marked in millimeters.

the 2W/kg whole-body-averaged specific absorption rate (SAR) inside the phantom.

In our FDTD simulation, to obtain E-field in phantom, a uniform mesh grid size of 15 mm was chosen along the x-, y-, and z-directions. The simulated electric field inside the phantom is shown in Fig. 6. The field closely conforms to the phantom profile. The field strength drops significantly from the edge of the

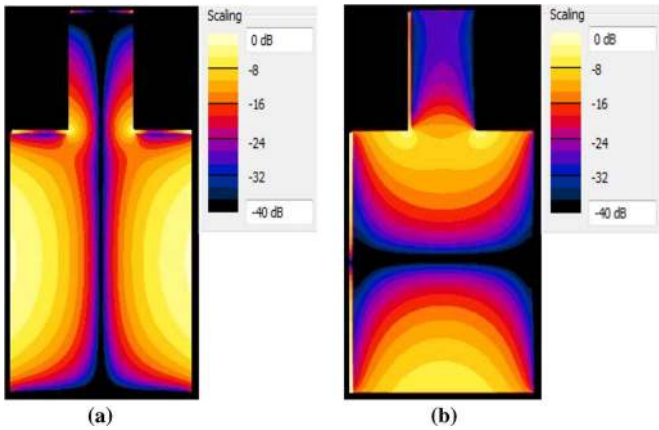

Fig. 7. Incident electric field distribution in decibels inside the ASTM phantom. (a) $\mathbf{E}_z$ field distribution on the vertical center plane. (b) $\mathbf{E}_x$ field distribution on the vertical center plane.

phantom to the center of phantom. The electric field obtained in this step is regarded as the incident field $\mathbf{E}_{\rm inc}$ in (7).

In the following sections, 17 different lead configurations placed inside the ASTM phantom are studied to validate our proposed approach.

1) Straight Lead Group: First we investigate the straight leads configuration. Three different lead lengths, L1, L2, and L3 as shown in Fig. 8, are investigated. These leads are also placed at different locations inside the phantom. The first lead is vertically placed in the phantom 4.5 cm (P1) away from the left side of the phantom. The second and the third leads (P2, P3) are moved 7.5 and 15 cm toward the center of the phantom, as shown in Fig. 8. Each position and length, $\mathbf{E}_{\rm tip}$ (denoted in Fig. 8 as a circle), was estimated by (7). For validation, we compare our method with the conventional FDTD method to directly calculate $\mathbf{E}_{\rm tip}$ for all nine cases. In these direct calculations, nonuniform meshes must be used. In the vicinity of the wires, the mesh size is on the order of millimeters. The mesh size increases for the regions that are away from the wire in order to make the problem solvable on regular computers. The maximum mesh size here is limited to 10 mm.

For the reciprocity approach, we use the currents $\mathbf{I}_L(l')$, shown in Fig. 5, together with the incident electric field $\mathbf{E}_{L,\rm inc}(l')$, shown in Fig. 7, to obtain $\mathbf{E}_{\rm tip}$ for all the positions shown in Fig. 8.

Comparisons are given in Table I. We found for all groups that the maximum error is only 4%. By further inspection, it can be seen for all three groups, the largest induced electric field is always at the P1 location and the smallest induced electric field is always at the P3 location. This phenomenon has been confirmed by the measurements in [9, Figs. 4(a) and 5(a)–(c)] and can be explained by inspecting the right side of (7). Considering current distributions $\mathbf{I}_L(l')$ almost identical, the tip electrode field will only rely on the strength of the local incident field. In Fig. 6, it is known that the electric field polarized along the vertical direction has the minimal values in the center region of the phantom. Therefore, the inner product of this low incident field with $\mathbf{I}_L(l')$ produces the smallest $\mathbf{E}_{\rm tip}$ value at P3. Finally, the tables show that the shortest line L_3 generates greater electric field than those from L_1 and L_2. This indicates that the longer

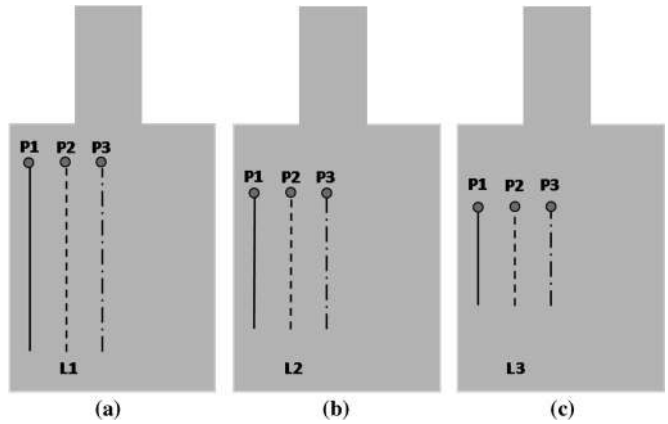

Fig. 8. Straight leads are put into the phantom at three positions (distance to the left border: P1 $= 4.5$ cm, P2 $= 12$ cm and P3 $= 19.5$ cm). (a) Lead length L1 $= 43.5$ cm. (b) Lead length L2 $= 28.5$ cm. (c) Lead length L3 $= 13.5$ cm.

TABLE I
COMPARISON OF SIMULATED $\mathbf{E}_{\rm tip}$ OF STRAIGHT LINE

		$\mathbf{E}_{tip}$ (V/m) / relative error (%)		
		P1	P2	P3
L_1	Direct	589	361	66
	This method	594 / 0.74	361 / 0.04	65 / 1.2
L_2	Direct	807	477	79
	This method	777 / 3.7	467 / 2.1	80 / 1.7
L_3	Direct	983	623	106
	This method	983 / 0.0	598/ 4.0	103 / 2.8

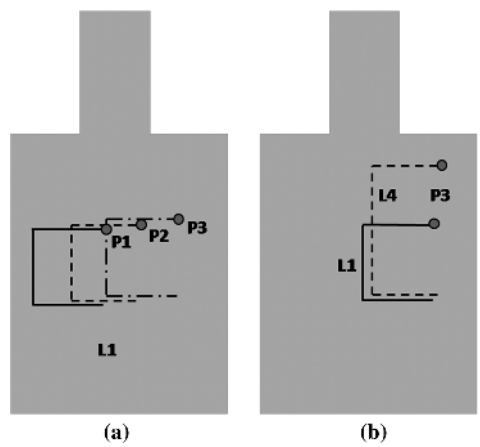

Fig. 9. Bended lead group is loaded into the phantom. (a) Lead length $L_1 = 43.5$ cm at three positions (distance to the left border: P1 $= 4.5$ cm, P2 $= 12$ cm and P3 $= 19.5$ cm). (b) Lead length $L_4 = 58.5$ cm at P3.

lead does not necessarily generate greater $\mathbf{E}_{\rm tip}$ due to possible phase cancellation effect.

2) Bended Lead Group: The second set of leads configuration considered here is to bend the upper and lower one-third of the straight lead L_1 in Fig. 8(a) into the horizontal directions to form a U-shape line, as shown in Fig. 9(a). In Fig. 9(b), we extended the lead at the P3 position in Fig. 9(a) by 15 cm towards the shoulder region of this phantom to make it longer.

Again, $\mathbf{E}_{\rm tip}$ is calculated by both direct simulation and the reciprocity approach, and the results are shown in Table II. Although the induced $\mathbf{E}_{\rm tip}$ on L_1 at P3 has the smallest value due to very small $\mathbf{E}_{\rm inc}$ over that area, changing its length by only 15 cm produces a much higher field in Table II. This is due to

TABLE II
COMPARISON OF SIMULATED $\mathbf{E}_{\rm tip}$ OF THE U-SHAPE LEADS, L_1 AND L_4

	$\mathbf{E}_{tip}$ (V/m) / relative error (%)			
	L1, P1	L1, P2	L1, P3	L4, P3
Direct	437	301	211	744
This method	425 / 2.8	303/ 1.5	222 / 5.2	743 / 0.2

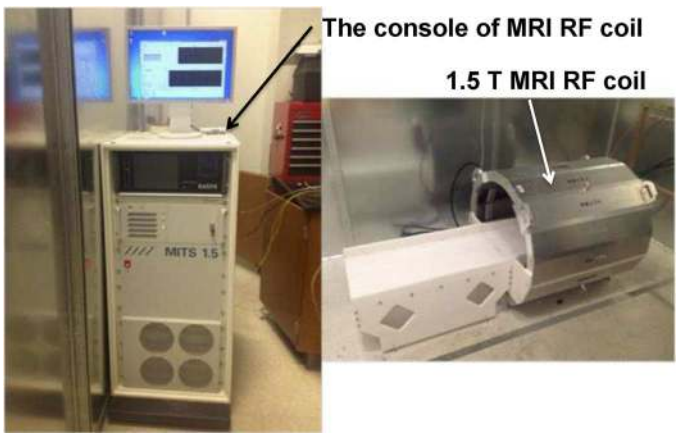

Fig. 10. Medical Implant Test System 1.5.

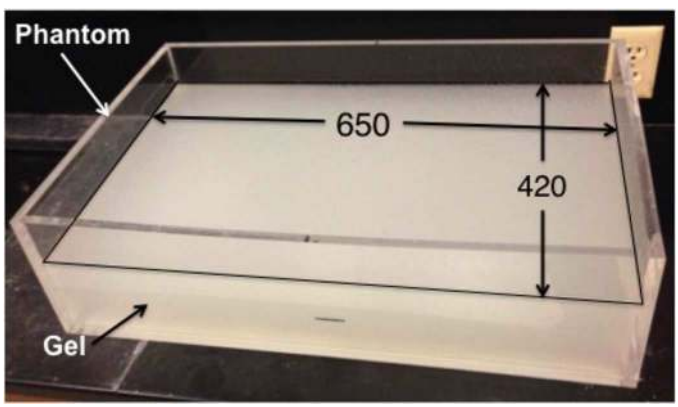

Fig. 11. Rectangular ASTM phantom filled with gel is used in the experiment. The dimensions of the phantom are marked in millimeters.

the field pattern in Fig. 7(a). The top shoulder region has very strong horizontal direction of $\mathbf{E}_{\rm inc}$ to interact with $\mathbf{I}_L(l')$.

B. Experimental Studies

In addition to performing the numerical studies above, experimental measurements were also carried out. In the experiments, the induced voltages at the ends of the devices were evaluated using the proposed method. The transfer function is measured first and then combined with the simulated incident field to estimate the induced electric field. The Medical Implant Test System MITS 1.5 (Zurich MedTech ZMT, Zurich, Switzerland), illustrated in Fig. 10, was used to emulate the RF exposure of the implant in MRI scanners. The system consisted of a 64-MHz birdcage coil that can be operated both in the linear and quadrature modes. A rectangular phantom was used in the measurement, as shown in Fig. 11.

The measurement validation was performed on two different wire structures, a four-wire cable and a coaxial cable. In each validation test, the induced voltages were found through direct

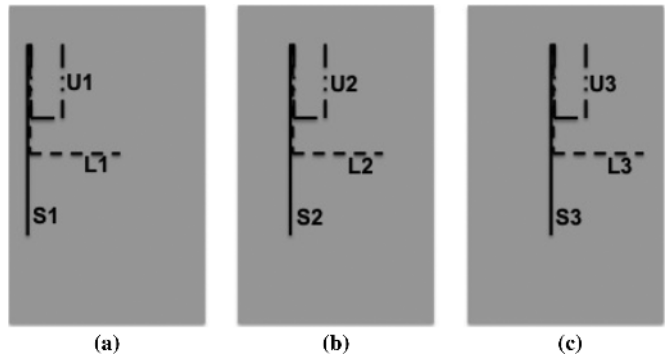

Fig. 12. Illustration of nine different trajectories for validation test (distance to the left border: S1, L1, and U1 are 2 cm; S2, L2, and U2 are 6 cm; S3, L3, and U3 are 10 cm. (a) Leads trajectories S1, L1, and U1. (b) Leads trajectories S2, L2. (c) Leads trajectories S3, L3, and U3.

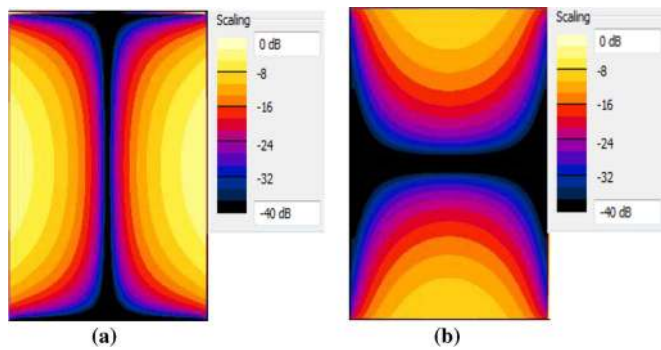

Fig. 13. Incident electric field distribution in decibels inside the rectangular ASTM phantom. (a) $\mathbf{E}_z$ field distribution on the vertical center plane. (b) $\mathbf{E}_x$ field distribution on the vertical center plane.

measurement and the reciprocity approach. Nine configurations as shown in Fig. 12 inside the phantom were used to evaluate the accuracy of this method. One set of lead paths was parallel to the phantom sidewall along the z-direction, and the other two lead path sets were U- and L-shaped paths to emulate conventional pectoral insertion and the sub-clavian lead insertions. Each set of lead paths consisted of three different offsets in the described configuration. The incident electric field distribution shown in Fig. 13 is extracted from simulation.

The four-wire cable investigated in this study is shown in Fig. 14. The length of the wire is 48 cm. Each wire is insulated from each other, and all these wires are encapsulated inside an outer insulator. A 3.6-Ω resistance is connected at one end of the cable between the two leads to model the pacemaker device CAN impedance. An SMA port is also connected to pick the induced voltage. The waterproof clay covered both the SMA port and the resistance.

The transfer function (common mode current distribution) of the four-wire cable is shown in Fig. 15. The transfer function obtained here is substituted into (7) together with the incident fields along nine different trajectories to estimate the induced voltage. Direct measurement was also performed by placing the four wires leads inside the ASTM phantom along the nine trajectories shown in previous figure. Fig. 16 shows the comparison between the directly measured and predicted results. As shown in the figure, the directly measured and predicted induced voltages match with each other very well. The largest induce voltage

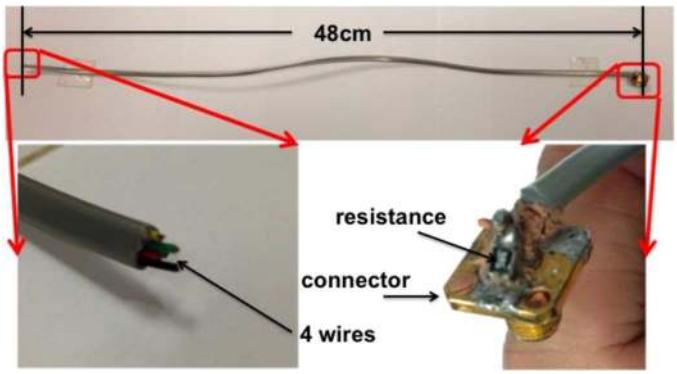

Fig. 14. Geometry and connector for the four-wire cable.

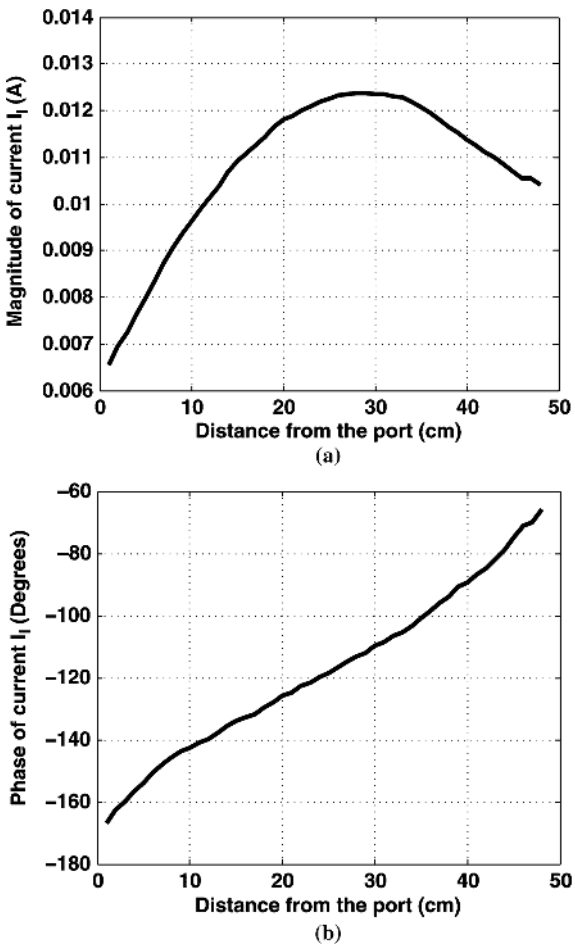

Fig. 15. Transfer function: (a) magnitude and (b) phase of the four-wire cable.

is about 0.5 V in S1 trajectory. The percentage error of the induced voltages on all trajectories is less than 20%.

In the second measurement validation, the induced voltage between the inner and outer conductor of a coaxial cable is studied as shown in Fig. 17. The same as the four-wire cable test, the length of the coaxial cable is also 48 cm. To model the pacemaker leads, which usually are covered by a plastic layer, the entire coaxial cable is covered by waterproof tape. The outer conductor was left off at one end of the coaxial cable. The other end of the coaxial cable is connected to an SMA port. A 3.6-Ω resistance is also connected between the inner and outer conductor to emulate the pacemaker device CAN impedance. The

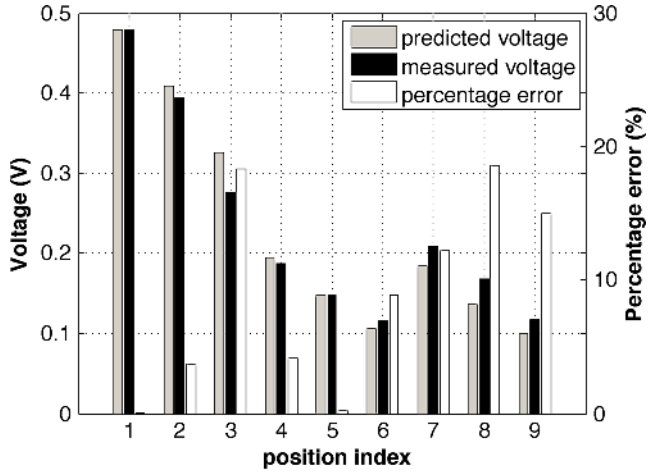

Fig. 16. Comparison between induced voltage from direct measurement and induced voltage predicted from transfer function for the four-wire cable.

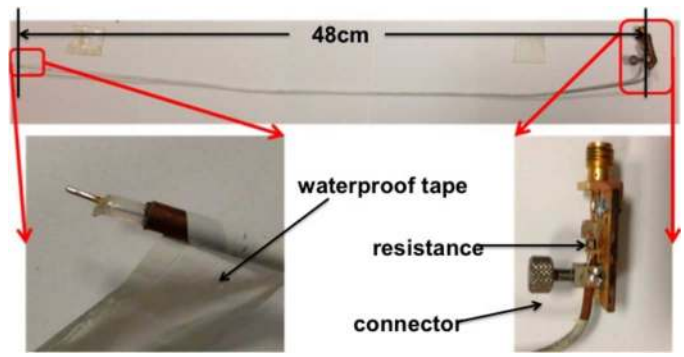

Fig. 17. Coax cable covered by a waterproof tape.

SMA connector, as well as the resistance were covered using clay during the measurement under the saline.

The transfer function of the coax structure is shown in Fig. 18, the same phantom as well as the pathway was used. Therefore, the same incident field is applied to the coaxial cable.

Fig. 19 shows the comparison between the measured and predicted results. As show in the figure, the largest induced voltage also appeared in the S1 trajectory. All the induced voltages for nine trajectories were consistent in both measured result and predicted result. The percentage error of the induced voltages on all trajectories is less than 20%.

By further examining (7), we deduce a very useful rule of thumb: the less energy is coupled from the tip electrode excitation onto the lead, the smaller $\mathbf{E}_{\text{tip}}$ is to be produced at the tip electrode. This implies that we can find ways to increase the transmission loss on the lead for a better MRI-compatible lead. Hence, this proposed method can be used as a testing procedure to investigate the effectiveness of newly developed MRI-compatible leads.

As discussed in Section I, it is computationally prohibitive to perform a complete lead, phantom/human subjects, and RF coil simulation all together even with the state-of-the-art electromagnetic modeling tools. This novel approach decouples the simulation/measurement of the lead characteristics from the human/phantom simulation. In this two-step procedure, one can carefully investigate the characteristic behaviors of the pacemaker leads using either simulation or measurement methods. Such information can be combined with conventional

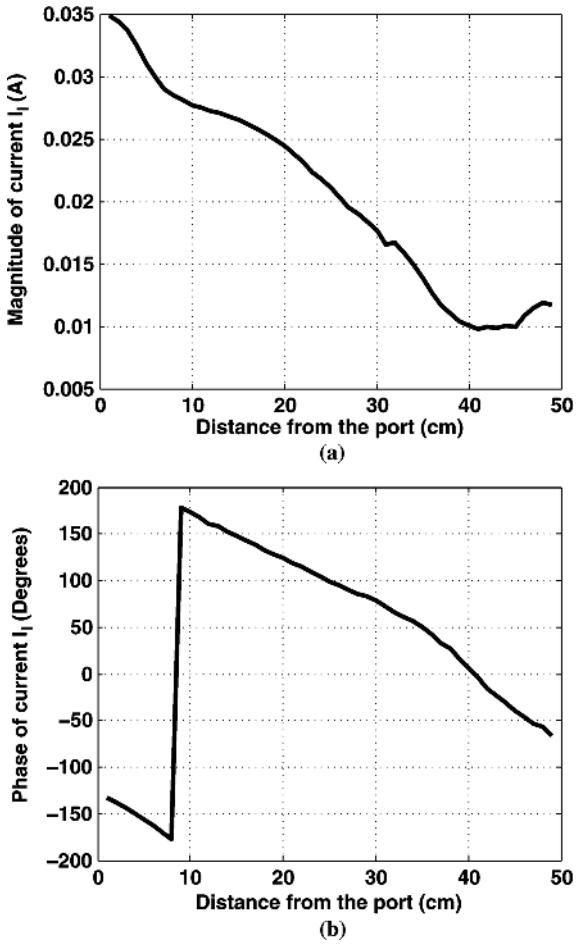

Fig. 18. Transfer function: (a) magnitude and (b) phase of the coax cable.

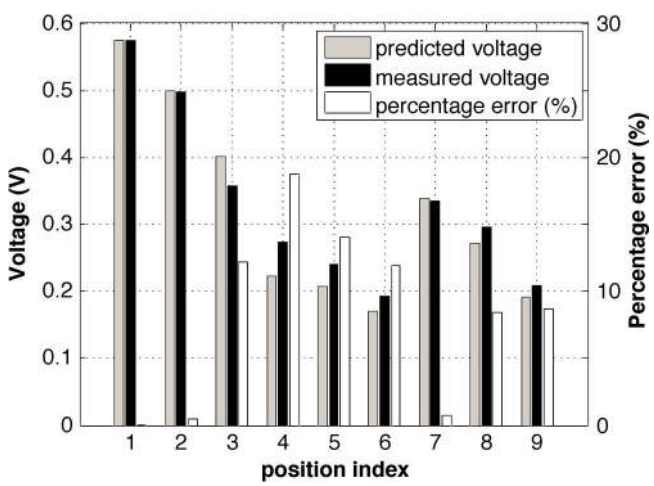

Fig. 19. Comparison between induced voltage from direct measurement and induced voltage predicted from transfer function for the coax.

human/phantom simulation results to estimate induced electric field for any lead trajectories. This is an practical technology that allows device manufactures to accurately estimate the induced electric field from the lead along any possible trajectories inside the human subject. It will lead to significant advancement in the MRI labeling area.

IV. Conclusions

In this paper, a novel approach to evaluate the MRI induced tip electrode electric field ($\mathbf{E}_{\rm tip}$) is proposed. Using the reciprocity theorem and the Huygens principle to de-couple the simultaneous simulation of the implanted lead, this approach significantly improves the efficiency of electromagnetic modeling. Examples are used to demonstrate the efficiency and accuracy of the proposed approach. The results indicate that the characteristics of an implanted lead ($\mathbf{I}_L$), as well as the incident electric field ($\mathbf{E}_{\rm inc}$) generated by the RF coil both have a significant impact on $\mathbf{E}_{\rm tip}$ of the implanted lead or induced voltage between different leads.

References

[1] J. R. Gimbel and E. Kanal, "Can patients with implanted pacemakers safely undergo magnetic resonance imaging?," *J. Amer. College Cardiol.*, vol. 43, no. 7, pp. 1325–1327, Apr. 2004.

[2] M. Fiek, T. Remp, C. Reithmann, and G. Steinbeck, "Complete loss of ICD programmability after magnetic resonance imaging," *Pacing Clin. Electrophys.*, vol. 27, no. 7, pp. 1002–1004, Jul. 2004.

[3] T. Azuma, K. Sasaki, K. Kawabata, A. Osada, H. Itagaki, K. Komura, T. Takahashi, K. Ishida, Y. Satoh, and S. Umemura, "MRI-compatible ultrasonic probe for minimally invasive therapy," in *IEEE Ultrason. Symp.*, Munich, Germany, Oct. 2002, vol. 2, pp. 1465–1468.

[4] S. Pisa, G. Calcagnini, M. Cavagnaro, E. Piuzzi, E. Mattei, and P. Bernardi, "A study of the interaction between implanted pacemakers and the radio frequency field produced by magnetic resonance imaging apparatus," *IEEE Trans. Electromagn. Compat.*, vol. 50, no. 1, pp. 35–42, Feb. 2008.

[5] S. Pisa, P. Bernardi, M. Cavagnaro, and E. Piuzzi, "Power absorption and temperature elevation produced by magnetic resonance apparatus in the thorax of patients with implanted pacemakers," *IEEE Trans. Electromagn. Compat.*, vol. 52, no. 1, pp. 32–40, Feb. 2010.

[6] S. Feng, R. Qiang, W. Kainz, D. R. Jackson, and J. Chen, "Efficient evaluation of MRI-induced electric fields in the vicinity of implantable lead," in *Wireless Microw. Circuits Syst. Symp.*, Waco, TX, USA, Apr. 2013, pp. 1–4.

[7] A. Roguin, M. M. Zviman, G. R. Meininger, E. R. Rodrigues, T. M. Dickfeld, D. A. Bluemke, A. Lardo, R. D. Berger, H. Calkins, and H. R. Halperin, "Modern pacemaker and implantable cardioverter/defibrillator systems can be magnetic resonance imaging safe: *in vitro* and *in vivo* assessment of safety and function at 1.5 T," *Circulation*, vol. 110, no. 5, pp. 475–482, Aug. 2004.

[8] C.-K. Chou, J. A. McDougal, and K. W. Chan, "RF heating of implanted spinal fusion stimulator during magnetic resonance imaging," *IEEE Trans. Biomed. Eng.*, vol. 44, no. 5, pp. 367–373, May 1997.

[9] E. Matttei, M. Triventi, G. Calcagnini, F. Censi, W. Kainz, G. Mendoza, H. I. Bassen, and P. Bartolini, "Complexity of MRI induced heating on metallic leads: Experimental measurements of 374 configurations," *Biomed. Eng. Online* Nov. 2008. [Online]. Available: http://www.biomedical-engineering-online.com/content/7/1/11

[10] J. A. Nyenhuis, S.-M. Park, R. Kamondetdacha, A. Amjad, F. G. Shellock, and A. R. Rezai, "MRI and implanted medical devices: Basic interactions with an emphasis on heating," *IEEE Trans. Device Mater. Rel.*, vol. 5, no. 3, pp. 467–480, Sep. 2005.

[11] E. Neufeld, S. Khn, G. Szekely, and N. Kuster, "Measurement, simulation and uncertainty assessment of implant heating during MRI," *Phys. Med. Biol.*, vol. 54, no. 13, pp. 4151–4169, Jul. 2009.

[12] M. G. Zanchi, R. Venook, J. M. Pauly, and G. C. Scott, "An optically coupled system for quantitative monitoring of MRI-induced RF currents into long conductors," *IEEE Trans. Med. Imag.*, vol. 29, no. 1, pp. 169–178, Jan. 2010.

[13] S.-M. Park, R. Kamondetdacha, and J. A. Nyenhuis, "Calculation of MRI-induced heating of an implanted medical lead wire with an electric field transfer function," *J. Magn. Reson. Imag.*, vol. 26, no. 5, pp. 1278–1285, Nov. 2007.

[14] E. Mattei, M. Triventi, G. Calcagnini, F. Censi, and P. Bartolini, "MRI in patients with implanted devices: A numerical model for the evaluation of lead heating," in *Proc. Comput. in Cardiol.*, Valencia, Spain, Sep. 2006, vol. 33, pp. 809–812.

[15] J. Nadobny, M. Szimtenings, D. Diehl, E. Stetter, G. Brinker, and P. Wust, "Evaluation of MR-induced hot spots for different temporal SAR modes using a time-dependent finite difference method with explicit temperature gradient treatment," *IEEE Trans. Biomed. Eng.*, vol. 54, no. 10, pp. 1837–1850, Oct. 2007.
[16] U. D. Nguyen, J. S. Brown, I. A. Chang, J. Krycia, and M. S. Mirotznik, "Numerical evaluation of heating of the human head due to magnetic resonance imaging," *IEEE Trans. Biomed. Eng.*, vol. 51, no. 8, pp. 1301–1309, Aug. 2004.
[17] L. Angelone, J. Ahveninen, J. W. Belliveau, and G. Bonmassar, "Analysis of specific absorption rate (SAR) at 3T MRI with variable deep brain stimulation (DBS) lead resistivity," *IEEE Trans. Med. Imag.*, vol. 29, no. 4, pp. 1029–1038, Apr. 2010.
[18] T. S. Ibrahim, "Ultrahigh-field MRI whole-slice and localized RF field excitations using the same RF transmit array," *IEEE Trans. Med. Imag.*, vol. 25, no. 10, pp. 1341–1347, Oct. 2006.
[19] E. Mattei, M. Triventi, G. Calcagnini, F. Censi, W. Kainz, H. I. Bassen, and P. Bartolini, "Temperature and SAR measurement errors in the evaluation of metallic linear structures heating during MRI using fluoroptic probes," *Phys. Med. Biol.*, vol. 52, no. 6, pp. 1633–1646, Feb. 2007.
[20] E. Mattei, G. Calcagnini, F. Censi, M. Triventi, and P. Bartolini, "Numerical model for estimating RF-induced heating on a pacemaker implant during MRI. Experimental validation," *IEEE Trans. Biomed. Eng.*, vol. 57, no. 8, pp. 2045–2052, Aug. 2010.
[21] T. Sommer, C. Vahlhaus, G. Lauck, A. von Smekal, M. Reinke, U. Hofer, W. Block, F. Trber, C. Schneider, J. Gieseke, W. Jung, and H. Schild, "MR Imaging and cardiac pacemakers: *in vitro* evaluation and *in vivo* studies in 51 patients at 0.5 T," *Radiology*, vol. 215, no. 3, pp. 869–879, Jun. 2000.
[22] P. Vernickel, V. Schulz, S. Weiss, and B. Gleich, "A safe transmission line for MRI," *IEEE Trans. Biomed. Eng.*, vol. 52, no. 6, pp. 1094–1102, Jun. 2005.
[23] C. J. Yeung, R. C. Susil, and E. Atalar, "RF safety of wires in interventional MRI: Using a safety index," *Magn. Reson. Med.*, vol. 47, no. 1, pp. 187–193, Jan. 2002.
[24] A. Christ, W. Kainz, E. G. Hahn, K. Honegger, M. Zefferer, E. Neufeld, W. Rascher, R. Janka, W. Bautz, J. Chen, B. Kiefer, P. Schmitt, H.-P. Hollenbach, J. Shen, M. Oberle, D. Szczerba, A. Kam, J. W. Guag, and N. Kuster, "The virtual familydevelopment of surface-based anatomical models of two adults and two children for dosimetric simulations," *Phys. Med. Biol.*, vol. 55, no. 2, pp. N23–N38, 2010.
[25] C. A. Balanis, *Advanced Engineering Electromagnetics*. New York, NY, USA: Wiley, 1989.
[26] J.-P. Berenger, "A huygens subgridding for the FDTD method," *IEEE Trans. Antennas Propag.*, vol. 54, no. 12, pp. 3797–3804, Dec. 2006.
[27] R. Luechinger, V. A. Zeijlemaker, E. M. Pedersen, P. Mortensen, E. Falk, F. Duru, R. Candinas, and P. Boesiger, "*In vivo* heating of pacemaker leads during magnetic resonance imaging," *Eur. Heart J.*, vol. 26, no. 4, pp. 376–383, Nov. 2005.
[28] *Standard Test Method for Measurement of Radio Frequency Induced Heating On or Near Passive Implants During Magnetic Resonance Imaging*, ASTM Standard F2182-11a, 2014.

Shi Feng (M'14) received the B.S. degree in electrical engineering from the Huazhong University of Science and Technology, Wuhan, China, in 2010, and is currently working toward the Ph.D. degree at the University of Houston, Houston, TX, USA.

His research interests include characterization of high-speed interconnects and numerical methods for periodic structures.

Rui Qiang (S'03–GSM'06–M'07), photograph and biography not available at time of publication.

Wolfgang Kainz (M'03) received the M.S. degree in electrical engineering and Ph.D. degree in technical science from the Technical University of Vienna, Vienna, Austria, in 1997 and 2000, respectively.

After working for the Austrian Research Center Seibersdorf (ARCS), he joined the Foundation for Research on Information Technologies in Society (IT'IS), Zurich, Switzerland, as an Associate Director. While with IT'IS, he was involved with the development of *in vivo* and *in vitro* exposure setups for bio-experiments. In 2004, he initiated the Virtual Family Project in cooperation with IT'IS and the University of Houston. He is currently a Senior Principal Scientist with the Food and Drug Administration (FDA), Center for Devices and Radiological Health, Silver Spring, MD, USA. His current research interests include the safety and effectiveness of medical devices and safety of humans in electromagnetic fields. This includes computational electrodynamics for safety and effectiveness evaluations using anatomical models of the human anatomy, MRI safety, performance and safety of wireless technology used in medical devices, electromagnetic compatibility (EMC) of medical devices, and dosimetric exposure assessments.

Dr. Kainz is the chairman of the IEEE International Committee on Electromagnetic Safety (ICES), Technical Committee 34, which develops compliance techniques for wireless devices. He is a member of the Administrative Committee, ICES. He was the recipient of the 2010 FDA's Award of Merit for exceptional leadership in performance in addressing issues of compatibility of medical devices during MRI by applying transparently scientific research to device regulation. The FDA's Award of Merit is the most prestigious honor award for exceptional performance and achievement that brought tribute to the FDA, Health and Human Services (HHS), or the Federal Government.

Ji Chen (SM'10) received the B.S. degree from the Huazhong University of Science and Technology, Wuhan, China, in 1989, the M.S. degree from McMaster University, Hamilton, ON, Canada, in 1994, and the Ph.D. degree from the University of Illinois at Urbana–Champaign, Urbana, IL, USA, in 1998, all in electrical engineering.

He is currently a Professor with the Department of Electrical Engineering, University of Houston, Houston, TX, USA. His research interests include microprocessor full chip-level interconnect extraction, wireless communication system-on-chip (SOC) interconnect characterization, computer system electromagnetic compatibility (EMC)/electromagnetic interference (EMI) modeling, signal integrity analysis, and bioelectromagnetics with applications to MRI systems.

Dr. Chen was the recipient of the Motorola Engineering Award in 2000 and the Oak Ridge Institute for Science and Education (ORISE) Fellowship in 2006.